Raman Spectroscopic Assessment of the Role of Parathyroid Hormone-related Protein on Bone Development in a Mouse Model

Michael Roberto

ABSTRACT

As part of a broader study of the uses of Raman spectroscopy to characterize the effects of metabolic diseases and genetic abnormalities on bone tissue, we have examined the tissue composition of transgenic mice with a defective parathyroid hormone-related protein (PTHrP). PTHrP plays an important role in normal development, especially in the regulation of bone formation and metabolism. A transgenic mouse model with a defective PTHrP gene sequence was used to assess the biological functions of this particular protein. These mice often do not survive longer than a few days and display abnormal skeletal features, including uncharacteristic bone and tooth morphology. To date, the role of PTHrP in bone or tooth composition has not been examined. The objective of this study was to investigate the effects of PTHrP on bone mineral and matrix properties with Raman spectroscopy by comparing transgenic mice with a deficient PTHrP gene sequence to wild type mice with a normal PTHrP sequence. Three groups of mice were examined: wild type (+/+, n=4), heterozygous (+/Δ, n=6), and homozygous (Δ/Δ , n=3). For each mouse, one tibia was sectioned at the mid-diaphysis to create two regions for Raman analysis. Raman spectra were acquired with an 830-nm system at both the proximal and distal ends of each tibial section to assess both cortical and cancellous bone tissue, which may be affected differently by the PTHrP mutation. Standard measures of bone composition, including mineral-to-matrix ratio, carbonate-to-phosphate ratio, and crystallinity, were computed and compared across the three groups. The PTHrP$^{\Delta/\Delta}$ mice exhibited the most pronounced skeletal abnormalities, and bone composition was most compromised in this group. Bone composition in the PTHrP$^{\Delta/+}$ mice was more similar to that of the PTHrP$^{+/+}$ mice but still exhibited defects in some metrics. This study is the first reported spectroscopic examination of bone composition in a mouse model of a genetic defect other than osteogenesis imperfecta. The results demonstrate that Raman spectroscopy may be generally useful for characterizing bone tissue composition abnormalities caused by genetic defects.

INTRODUCTION

Bone is a highly organized living tissue, composed of mineral, organic matrix, and water. The bone mineral consists mostly of apatitic crystals and often contains impurities, such as carbonate substitutions, in the crystal lattice. The mineral contributes to the rigidity and compressive strength of bone. The bone matrix is composed primarily of type I collagen with small amounts of proteoglycans and noncollagenous proteins. Collagen provides flexibility and tensile strength to bone, as well as nucleation loci where the mineral crystals can form. The proteoglycans and noncollagenous proteins play a role in the assembly of collagen in unmineralized bone matrix, or osteoid, and the subsequent mineralization of this new bone [1].

On a larger scale, bone is organized into either cortical bone, found along the shafts of long bones and in the shell surrounding vertebrae, or cancellous bone, found in the ends of long bones and in vertebrae and flat bones. Cortical bone is very dense, with a porosity of 5-10%, while cancellous bone is more porous, with a porosity of 75-95% (Figure 1). The structure and porosity of bone changes and adapts during skeletal development and over time in response to many stimuli, such as disease, injury, drug therapy, and exercise or other mechanical loading. These changes may affect bone at many levels, including the whole bone strength and the tissue architecture, material properties, and composition.

Bone tissue can be characterized using a variety of techniques. Bone mineral density (BMD), a measure of the amount of mineral present in bone tissue, is the most common clinical metric used to assess a patient's risk for sustaining a skeletal fracture. Dual-energy X-ray absorptiometry (DXA) is the current gold standard for measuring BMD and assessing fracture risk noninvasively, although it only provides two-dimensional information, or *areal* BMD. Quantitative computed tomography (QCT), another X-ray technique, measures *volumetric* BMD, as well as cortical bone geometry and cancellous bone architecture. However, QCT lacks the spatial resolution to detect small changes in geometry and architecture. Magnetic resonance imaging (MRI) can also measure mineral density, geometry, and architecture in bone and has the added advantage of non-ionizing radiation. All of these methods are powerful and yield valuable information about BMD, geometry, and architecture, but bone integrity is based on more than these properties alone. A key component to bone integrity that these other techniques are not able to probe is the chemical composition and chemical structure of bone mineral and matrix Raman spectroscopy is one way to obtain this information and is currently the only method being developed for noninvasive measurements of bone composition.

Raman spectroscopy and infrared (IR) spectroscopy are forms of vibrational spectroscopy used to examine the chemical structure of various compounds. IR spectroscopy is based on light absorption of the different chemical species within a compound. Water absorption creates strong interference, limiting IR spectroscopy to penetration depths less than 100 microns. Raman spectroscopy is a light scattering technique wherein specimens are excited with visible or near-IR lasers. Therefore, water is rendered nearly invisible in Raman spectra, making this technique ideal for fresh biological specimens that must be kept hydrated. In addition, the glass and fused silica optics commonly used with biological specimens yield little or no signal in the near-IR region.

Vibrational spectroscopy provides insight into the chemical composition of bone, which is an important contributor to bone quality [2]. Raman spectra of bone tissue have distinct bands characteristic of the mineral and matrix components (Figure 2). Phosphate and carbonate symmetric stretches are the two strongest mineral bands at 959 cm^{-1} and 1070 cm^{-1} respectively. The carbonate-to-phosphate ratio changes in response to local perturbations of the crystal structure. The inverse of the full width at half maximum (1/fwhm) of the phosphate band represents bone mineral crystallinity and is a measure of lattice order. A narrow phosphate band, corresponding with high crystallinity, indicates large crystals and low lattice strain. Carbonate substitution induces structural distortions in the lattice, which affects the crystallinity. Matrix bands include proline at 850 cm^{-1}, hydroxyproline at 873 cm^{-1}, phenylalanine at 1002 cm^{-1}, and an amide I envelope in the 1600-1700 cm^{-1} region. Proline, hydroxyproline, and phenylalanine bands are measures of collagen content that are relatively insensitive to changes in the secondary structure. The amide I envelope, however, is sensitive to the degree of crosslinking in the collagen fibrils. Collagen crosslinking is tied to collagen maturity and is determined by the ratio of the 1662 cm^{-1} band to the 1685 cm^{-1} band within the amide I envelope. The crosslinking ratio increases with collagen maturity. Bone mineral content is assessed using the mineral-to-matrix ratio, calculated using the phosphate ν_1 band and any of several matrix bands, including proline and amide I at 1662 cm^{-1}.

Measurable changes occur in both the mineral and matrix bands when bone is permanently or elastically deformed, as shown by previous studies in this laboratory [3-5]. Chemical composition also varies with osteoporotic fracture, as evidenced by differences between the Raman spectra of femoral bone in women that fractured and women that did not fracture [6]. In this study, the carbonate/phosphate band area ratio was approximately 20% higher in the fractured bone tissue. In addition, Raman spectroscopy has been used to characterize changes in bone tissue composition associated with osteogenesis imperfecta, a genetic disorder that affects bone matrix [7]. These and other studies suggest that Raman spectroscopy can play an important role in the study of bone tissue, especially with genetic defects that produce abnormal bone composition.

Many transgenic animal models have been developed to study the physiologic factors that influence skeletal development and adaption [8]. These models are mostly used to mimic a particular human disease and study its effects in a homogeneous population or to study the function of a particular gene. Many different proteins contribute to the development and aging of bone tissue. In particular, the parathyroid hormone (PTH)-related protein (PTHrP) plays an important role in many physiological tasks, including cell proliferation, differentiation, and apoptosis. PTHrP regulates many skeletal functions, such as endochondral bone formation and tooth eruption, by binding to the PTH-1 receptor via the N-terminus of the molecule [9]. However, previous *in vitro* experiments by our collaborators in the laboratory of Prof. Ramiro Toribio (College of Veterinary Medicine, Ohio State University) have indicated that PTHrP may mediate some cell functions via the molecule mid-region, nuclear localization sequence (NLS), and C-terminus [10]. To examine the effects of these three regions on skeletal development the Toribio laboratory created a knock-in mouse model using homologous recombination to replace the full-length PTHrP sequence with one lacking the coding region for amino acids 67-137. Two mouse groups were developed, one completely lacking the coding region for amino acids 67-137 ($\text{PTHrP}^{\Delta/\Delta}$) and one lacking the region only in one allele ($\text{PTHrP}^{\Delta/+}$). Using Raman spectroscopy to determine bone composition of these varying genotypes, we are able to examine the role of the PTHrP gene in bone development.

EXPERIMENTAL METHODS

Specimen Preparation

The PTHrP knock-in mice and wild type littermates were sent from the Toribio laboratory to our collaborators in the laboratory of Prof. Laurie McCauley (Department of Periodontics and Oral Medicine, School of Dentistry, University of Michigan), where they were sacrificed for tissue harvest. We received the hindlimbs of 13 mice from the McCauley laboratory (Table 1). The mice were from three experimental groups based on the knock-in model described above: homozygous ($PTHrP^{\Delta/\Delta}$, n=3), heterozygous ($PTHrP^{\Delta/+}$, n=6), and wild type ($PTHrP^{+/+}$, n=4). All mice were less than one month old. The $PTHrP^{\Delta/\Delta}$ mice all died at a neonatal stage, two of them dying before three days. Prior to the Raman measurements the mouse hindlimbs were wrapped in gauze soaked with phosphate buffered saline (PBS) and stored at -20°C.

Because the hindlimbs were small, a custom video system constructed from an arthroscope and camera was used to obtain a magnified image of the bone. With magnification, the hindlimb anatomy was visible with adequate detail for dissection and sectioning. Each hindlimb was thawed to room temperature, and some skin and muscle tissue were carefully removed using a scalpel so that the bone could be visualized more clearly. The tibia was sectioned into two segments by making three transverse cuts (Figure 3). The cuts were made by holding the tibia with a pair of tweezers and sawing lightly through the bone using a scalpel. The cuts were performed slowly, holding the scalpel blade perpendicular to the diaphysis, and with very light pressure to avoid damaging the fragile bone. Extra care was required for the $PTHrP^{\Delta/\Delta}$ mice, as those bones were the most fragile. The first cut was made in the proximal tibial metaphysis, distal to the growth plate, to expose cancellous bone. Similarly, the second cut was made in the distal metaphysis, proximal to the growth plate, to expose cancellous bone. The third cut was made at the mid-diaphysis, to expose cortical bone. After excising the tibia segments, any remaining skin and muscle were carefully separated from the bone.

Raman Spectroscopy

The sectioning procedure produced four exposed bone surfaces per tibia to examine with Raman spectroscopy: 1) proximal segment cancellous bone, 2) proximal segment cortical bone, 3) distal segment cortical bone, and 4) distal segment cancellous bone. For the Raman measurements, the bone segment was placed on a tissue on top of a glass microscope slide measuring 3 in x 1 in x 1 mm (Fisher Scientific, Pittsburgh, PA). Because the bone surfaces were small, Raman spectra were sampled across the entire cross-section (Figure 4). An acquisition time of 5 minutes was used. The mice specimens were examined in random order (Table 1).

Raman System

The Raman spectra were collected using a custom Raman system consisting of a commercial benchtop Raman analyzer (RXN1, Kaiser Optical Systems, Inc., Ann Arbor, MI), an upright microscope (Eclipse ME600, Nikon Instruments, Inc., Melville, NY), and various beam-shaping optics (Figure 5). Within this setup, a 400-mW, 830-nm diode laser was focused into a fused silica multimode optical fiber with a 100-µm diameter core. The fiber was launched into a fiber coupler assembly with a built-in fiber positioner (F-91-C1-T, Newport Corp., Irvine, CA) and a 10x/0.50 numerical aperture objective (Fluar, Carl Zeiss Microimaging, Inc., Thornwood, NY). The laser light was collimated using an air-spaced doublet collimator (F810FC-780, ThorLabs, Newton, NJ), shaped into a line (1° fan angle Powell lens, Lasiris, St-Laurent, Québec), focused with achromat lenses, and then reflected by a dichroic mirror (R830RDC, Chroma Technology Corp., Rockingham, VT) into the microscope. A 20x/0.75 numerical aperture fluorescence resistant objective (S Fluor, Nikon Instruments, Inc., Melville, NY) focused the laser line onto the sample. A neutral density filter with an optical density of 0.2 was used to attenuate the laser beam and avoid specimen burning for most specimens (Appendix A lists the specimens for which the filter was used).

Raman-shifted scatter was collected through the same objective, transmitted through the dichroic mirror, and focused by an achromatic lens with a 60-mm focal length (AC254-060-B, Thorlabs) onto a rectangular bundle of 50 optical fibers (custom assembly, FiberTech Optica, Inc., Kitchener, Ontario, Canada). The collection bundle consisted of a set of 50 near-infrared (NIR) optical fibers with a 100-μm diameter core that were arranged into a 5x10 close-packed array at the input end and a 1x50 linear array at the termination end. Each fiber contained a fused silica core, surrounded by fluorine-doped fused silica cladding (110-μm diameter) and a polymide buffer (125-μm diameter). The buffer was stripped from the fibers at each end of the collection bundle. The linear fiber array delivered the collected Raman scatter to a NIR-optimized imaging spectrograph fitted with a 50-μm slit to provide a spectral resolution of 6-8 cm^{-1}. The light was then dispersed onto a thermoelectrically-cooled, deep-depletion, 1024x255 pixel CCD operated at -40°C. A frame-grabber board and support software were used with a video camera to capture images of the surface where the laser was focused.

Data Processing

The raw data (Figure 6) were arrays of 255 Raman spectra collected as single CCD images. All data processing was performed in MATLAB (R2008b, The

Mathworks, Inc., Natick, MA) using custom written scripts (Appendix B). Preprocessing of the Raman spectra included correcting the image curvature resulting from spectrograph astigmatism produced at the slit, removing cosmic rays and other spikes, and subtracting the dark current. Spectral wavelength and intensity were calibrated using neon and white-light sources, respectively (Raman Calibration Accessory, Kaiser Optical Systems, Inc.). The wavelength axis was calibrated by comparing the neon spectra with reference values from the National Institute of Science and Technology (NIST). After preprocessing the spectra were truncated to include a wavenumber region of interest (ROI) from 838 cm^{-1} to 1723 cm^{-1} (Figure 7). The fluorescence background was removed using a modified polynomial baselining script, which baselined each row of data from the CCD separately and then summed along the wavenumber axis to produce the final spectrum (Figure 8). All spectra were normalized to the maximum intensity of the phenylalanine band.

Peak fitting was performed in GRAMS (Thermo Fisher Scientific, Waltham, MA) using three spectral regions to characterize the composition of the mineral and matrix components of bone tissue. The region surrounding phosphate ν_1 (900-991 cm^{-1}) was fitted with three peaks at 920, 937, and 959 cm^{-1}, with 959 cm^{-1} representing the phosphate ν_1 band used in band intensity calculations. The region surrounding carbonate (991-1135 cm^{-1}) was fitted with five peaks at 1003, 1035, 1048, 1073, and 1103 cm^{-1}, with 1073 cm^{-1} representing the carbonate band utilized in calculations. The region surrounding amide I (1520-1700 cm^{-1}) was fitted with 6 peaks at 1565, 1585, 1602, 1620, 1639, and 1662 cm^{-1}, with 1662 cm^{-1} representing the amide I band in intensity calculations. The band intensities of the fitted peaks were measured, and various band intensity ratios were computed, namely phosphate-to-amide I, phosphate-to-phenylalanine, phosphate-to-carbonate, 1690 cm^{-1}-to-1660 cm^{-1} bands of Amide I, and phosphate-to-proline. In addition, the mineral crystallinity (1/fwhm) was computed using the phosphate ν_1 band at 959 cm^{-1}.

The computed Raman measures were compared across the three experimental groups ($PTHrP^{\Delta/\Delta}$, $PTHrP^{\Delta/+}$, $PTHrP^{+/+}$) using repeated measures analysis of variance (ANOVA) with the SAS statistical software (SAS 9.1, SAS Institute, Inc., Cary, NC). . The analyses treated the four measurement sites within the bone as the repeated measure and were performed using a mixed-effect model with an unstructured covariance structure. Pairwise comparisons were made between the groups using a Tukey-Kramer adjustment for multiple comparisons. Various influence diagnostics were used to identify outliers, which were then excluded from the analyses. A significance level of 0.05 was used for all statistical analyses.

Results and Discussion

The bone mineral content differed significantly among the three mouse genotypes, as measured by the phosphate-to-phenylalanine and phosphate-to-amide I ratios ($p < 0.0001$ for both, Figure 9). $PTHrP^{\Delta/\Delta}$ mice had a lower phosphate-to-phenylalanine ratio than either $PTHrP^{\Delta/+}$ or $PTHrP^{+/+}$ mice ($p = 0.003$ and $p < 0.0001$, respectively), and $PTHrP^{\Delta/+}$ mice had a lower ratio than $PTHrP^{+/+}$ mice ($p < 0.0001$). Similarly, the phosphate-to-amide I ratio was lower in both $PTHrP^{\Delta/\Delta}$ and $PTHrP^{\Delta/+}$ mice than in $PTHrP^{+/+}$ mice ($p < 0.0001$ for both). This ratio tended to be lower in $PTHrP^{\Delta/\Delta}$ mice than in $PTHrP^{\Delta/+}$ mice, although this difference was not significant ($p = 0.07$). The phosphate-to-proline ratio did not yield conclusive results. Overall, these results indicate that the bone tissue of homozygous mice was less mineralized than either the heterozygous or wild type mice. Mineralization in the heterozygous mouse was generally lower than normal, although the difference was not always detectable. Because perturbation of the PTHrP gene induced these changes in the mineral-to-matrix ratio, PTHrP seems to play a substantial role in bone mineralization during development.

Genotype differences were also observed in the quality of the bone mineral, measured by crystallinity ($p = 0.001$) and the carbonate-to-phosphate ratio ($p < 0.0001$, Figures 10, 11). Multiple comparisons revealed that crystallinity was lower in PTHrP$^{\Delta/\Delta}$ mice than in PTHrP$^{\Delta/+}$ and PTHrP$^{+/+}$ mice ($p = 0.02$ and $p = 0.007$, respectively), indicating smaller and less perfect mineral crystals. Crystallinity did not differ between PTHrP$^{\Delta/+}$ and PTHrP$^{+/+}$ mice ($p = 0.3$). In addition, PTHrP$^{\Delta/\Delta}$ mice had greater carbonate content than either PTHrP$^{\Delta/+}$ or PTHrP$^{+/+}$ mice ($p = 0.01$ and $p < 0.0001$, respectively) and PTHrP$^{\Delta/+}$ mice had greater carbonate than PTHrP$^{+/+}$ mice ($p < 0.0001$). The values of the carbonate-to-phosphate ratios were large, ranging from 34 to 56%. Because these mice were very young, and the bone tissue should be lightly carbonated, the elevated ratios likely result from an overlap between carbonate ν_1 at 1073 cm^{-1} and phosphate ν_3 at 1076 cm^{-1} that could not be resolved. However, carbonate content generally tracks crystallinity in relation to the strong phosphate ν_1 band, and similar trends were observed here in the two measures. Overall, the quality of the mineral lattice in the homozygous mice was generally lower than in heterozygous or wild type mice. The origin of these differences is unknown; the lower quality in PTHrP$^{\Delta/\Delta}$ mice may result from a compromised ability to mineralize bone or merely from a younger age. Because the

PTHrP$^{\Delta/\Delta}$ mice failed to thrive more than a couple of days postnatally, the lattice structure had less time to mature than in the other mice.

The maturity of collagen crosslinks differed by genotype ($p < 0.0001$). The crosslinking ratio was lower in PTHrP$^{\Delta/\Delta}$ mice than PTHrP$^{\Delta/+}$ mice ($p = 0.04$), indicating less mature collagen crosslinks in the heterozygous mice. The variance in these data was large, which limited the ability to detect differences between groups. The 1690 cm^{-1} band could not be repeatably resolved, because it lies at the edge of detection for the CCD, which has low quantum efficiency in that spectral region for the 830-nm excitation wavelength. Therefore, the crosslinking results were mostly inconclusive.

The signal-to-noise ratio, calculated at locations near the phosphate ν_1 band, averaged 36.9 ± 31.9 (range = 3.91-147). The low signal-to-noise ratio can be attributed to the neonatal stage of all mice, which had little time for mineralization. As a result, Raman measurements were averaged over regions with little mineral and regions with much more mineral, yielding large variances. The signal-to-noise ratio decreased at higher wavenumbers. A band should be visible at 1690 cm^{-1}, but the quantum efficiency of the CCD falls off in that region and is at the edge of its detection.

The fragile PTHrP$^{\Delta/\Delta}$ bone tissue burned under the laser beam. The problem was observed with the first homozygous specimen examined and solved with the addition of a neutral density filter to attenuate laser power. The damaged region of that specimen was not used for additional measurements, because the tissue was burned. Repeat measurements were not performed in specimens that were previously examined, because the tissue was compromised. The neutral density filter was used for all subsequent measurements. Consequently, the final data set includes spectra acquired both with and without the filter. Absolute intensity variations caused by differences in the total incident laser energy and instrument optical alignment were cancelled out when the spectra were normalized by the intensity of the phenylalanine band.

Spectral baselining was performed through many iterations to improve the final spectrum. The baselining script used originally was not robust enough to handle spectra that had very small arbitrary intensities, resulting in a noticeable offset that compromised fitting. Subsequently, a custom script was used to fit the peaks. Although this script has proven useful in other situations, the larger amount of noise present in this experiment yielded fits that were unreliable and not repeatable. Therefore, only fits performed in GRAMS were retained.

Conclusions

In general, the bone tissue of PTHrP$^{\Delta/\Delta}$ mice was significantly compromised, resulting in reduced mineral content, lower crystallinity, and higher carbonate content compared to wild type mice. The bone tissue of PTHrP$^{\Delta/+}$ mice was also negatively affected. Decreased bone integrity with increased expression of compromised PTHrP was observed across multiple Raman metrics, especially in the mineral-to-matrix and carbonate-to-phosphate ratios. Combined with the severe skeletal abnormalities and physical fragility of the bone, these results suggest that PTHrP plays a key role in skeletal development, especially in mineral formation and crystal growth.

Table 1. Specimen information. The order in which specimens were examined is given by specimen number.

Specimen number	Specimen ID	Genotype
1	J9 +/- #1	heterozygous
2	M8 +/- #3	heterozygous
3	M10 +/- #2	heterozygous
4	M10 +/+ #3	wild type
5	E10 -/-	homozygous
6	M9 +/- #2	heterozygous
7	C10 +/+ #6	wild type
8	M10 -/- #1	homozygous
9	C10 +/+ #5	wild type
10	E10 +/-	heterozygous
11	C8 +/+ #2	wild type
12	B9 -/-	homozygous
13	M9 +/- #1	heterozygous

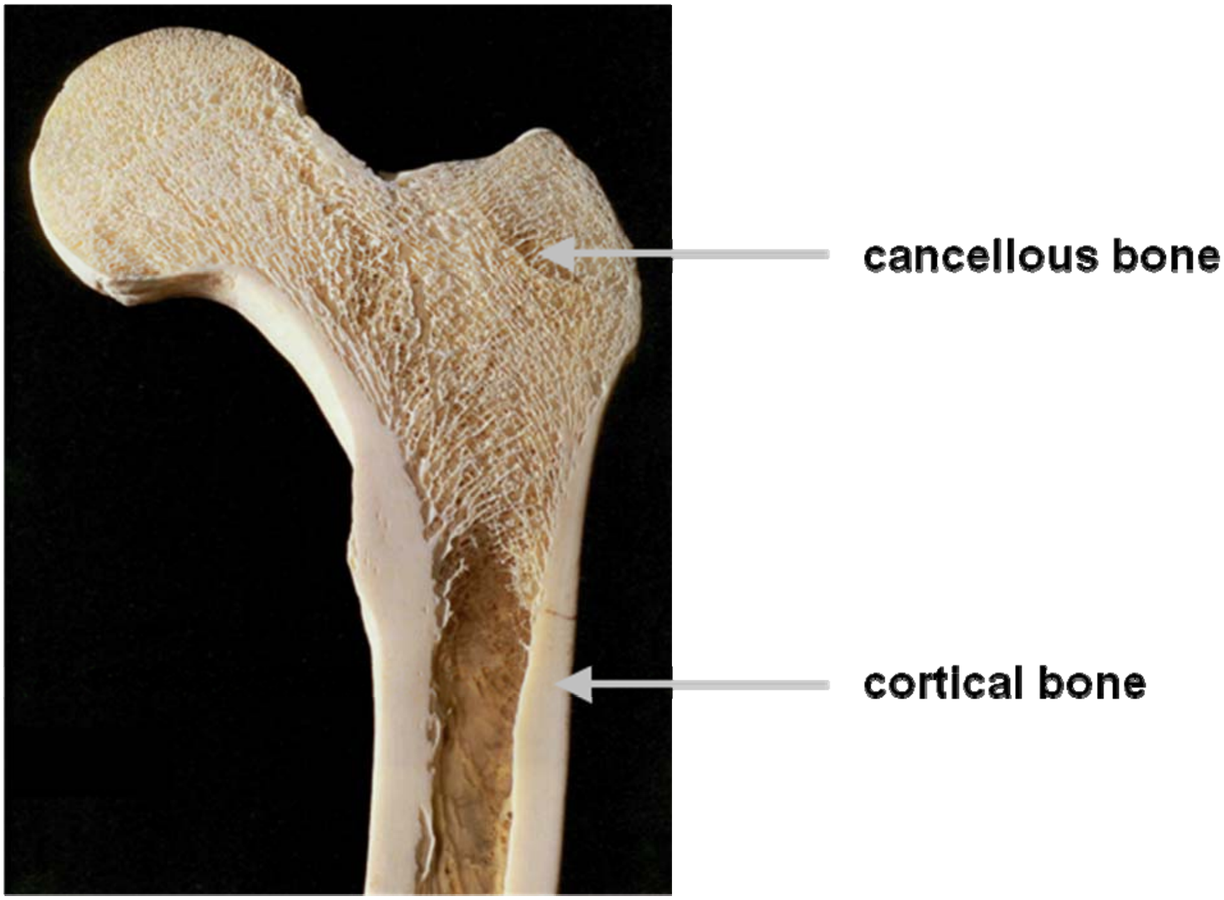

Figure 1. Upper portion of a human femur cut lengthwise to expose the cortical and cancellous bone regions (from Plate 37 in ref. [11])

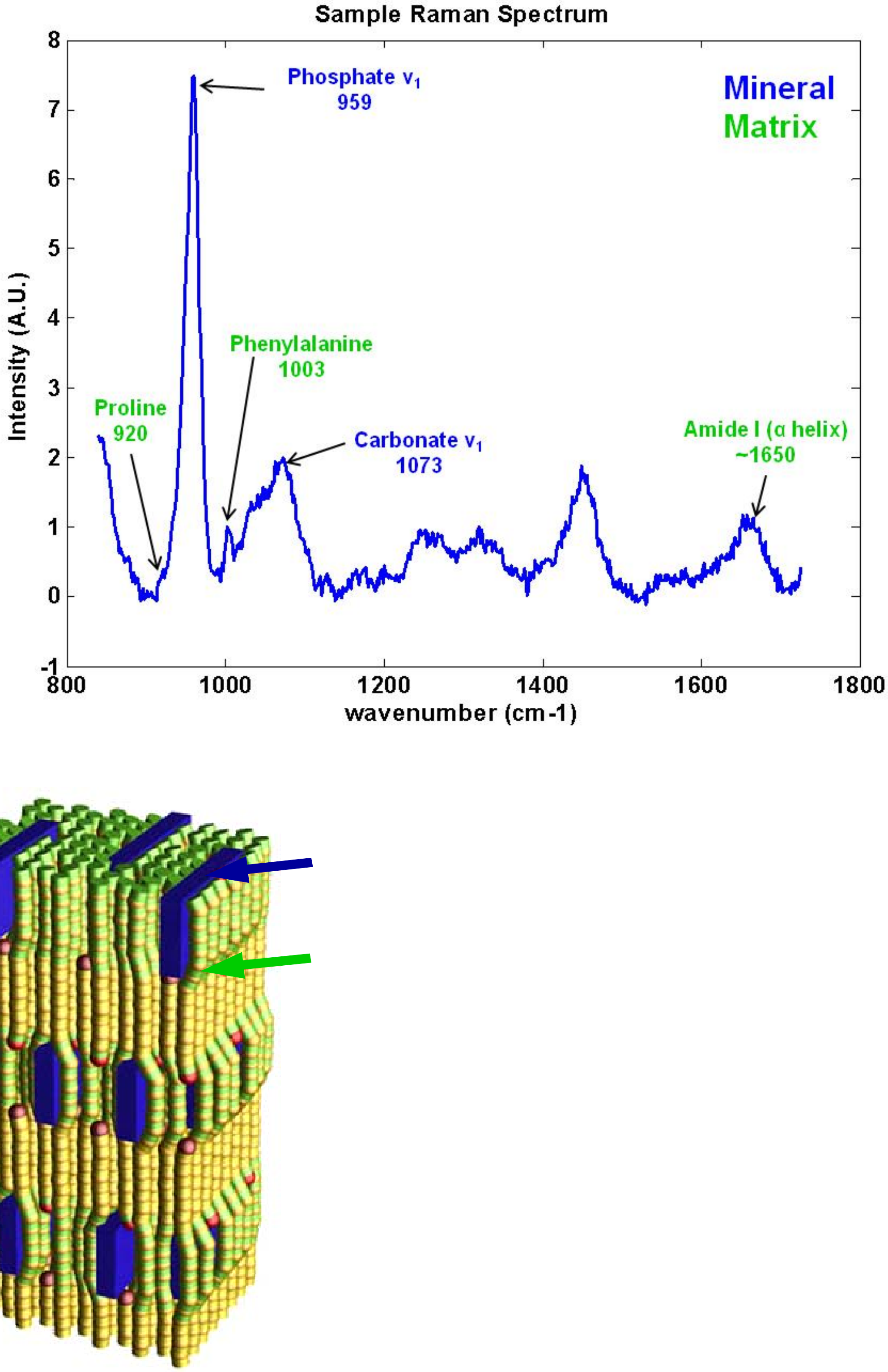

Figure 2. Top: Sample Raman spectrum of bone showing important mineral and matrix bands. Bottom: a schematic diagram of bone tissue illustrating the collagen fibrils (green arrow) that are embedded with mineral crystallites (blue arrow).

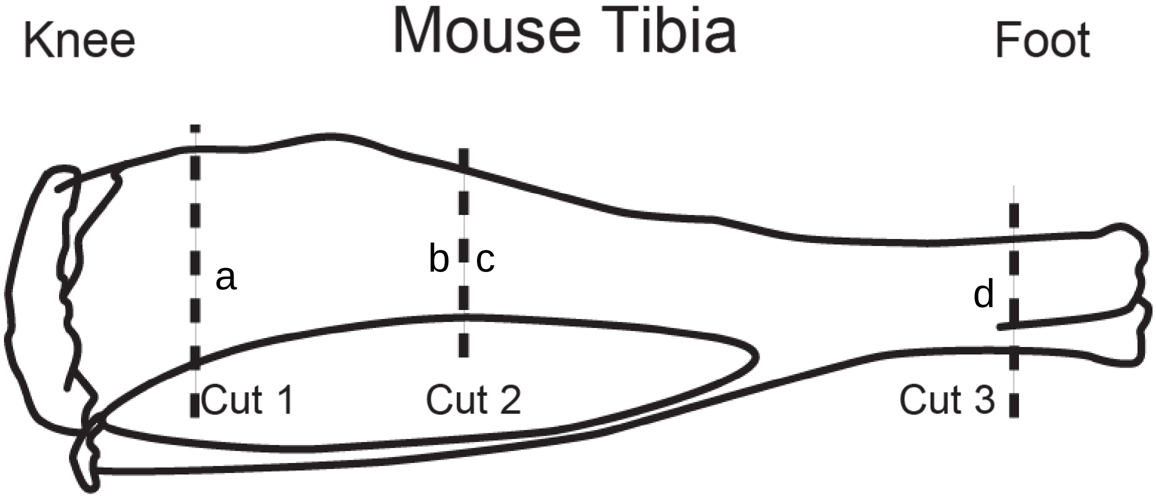

Figure 3. Tibial segments created by making three transverse cuts. Sampling sites shown by letters a, b, c, and d. Sites a and d are cancellous bone, while b and c are cortical bone.

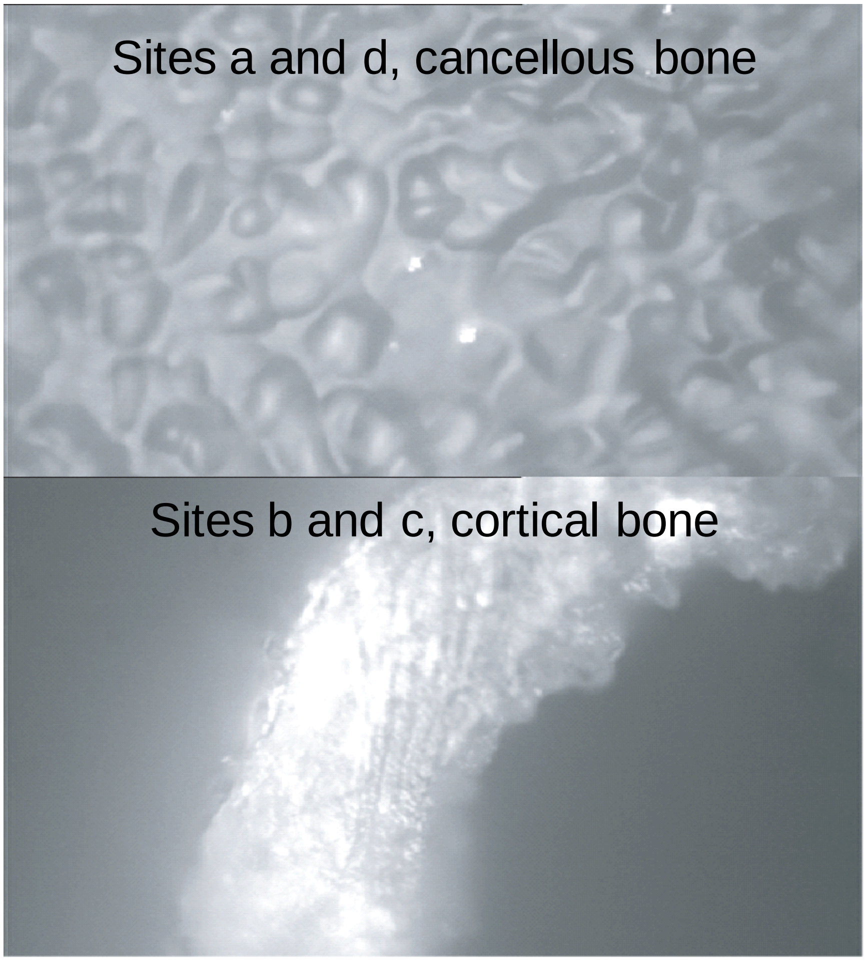

Figure 4. Sample images of cancellous and cortical bone from the mouse tibia. Sites defined in Figure 3.

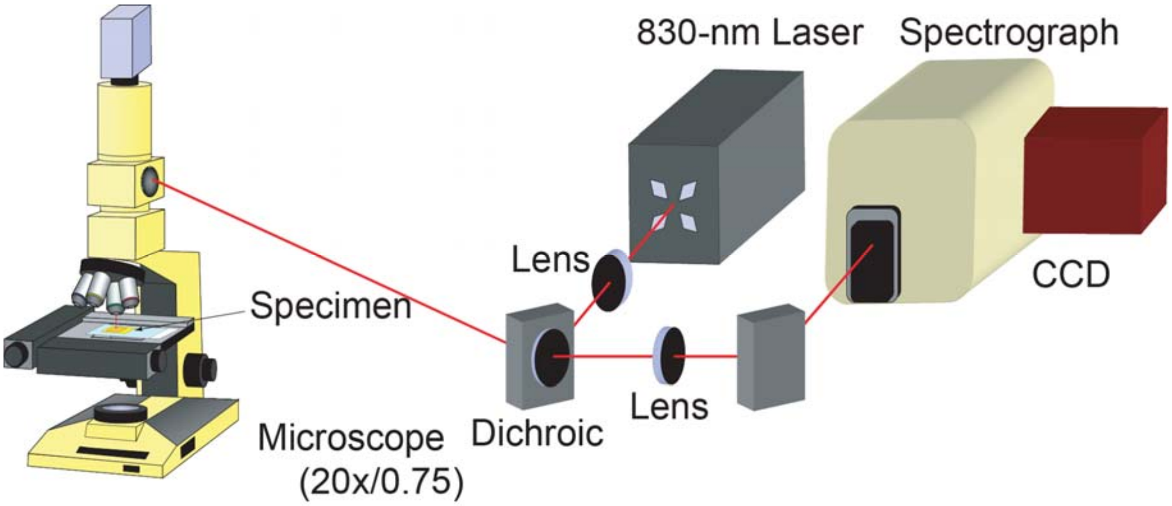

Figure 5. Schematic of Raman spectroscopic apparatus.

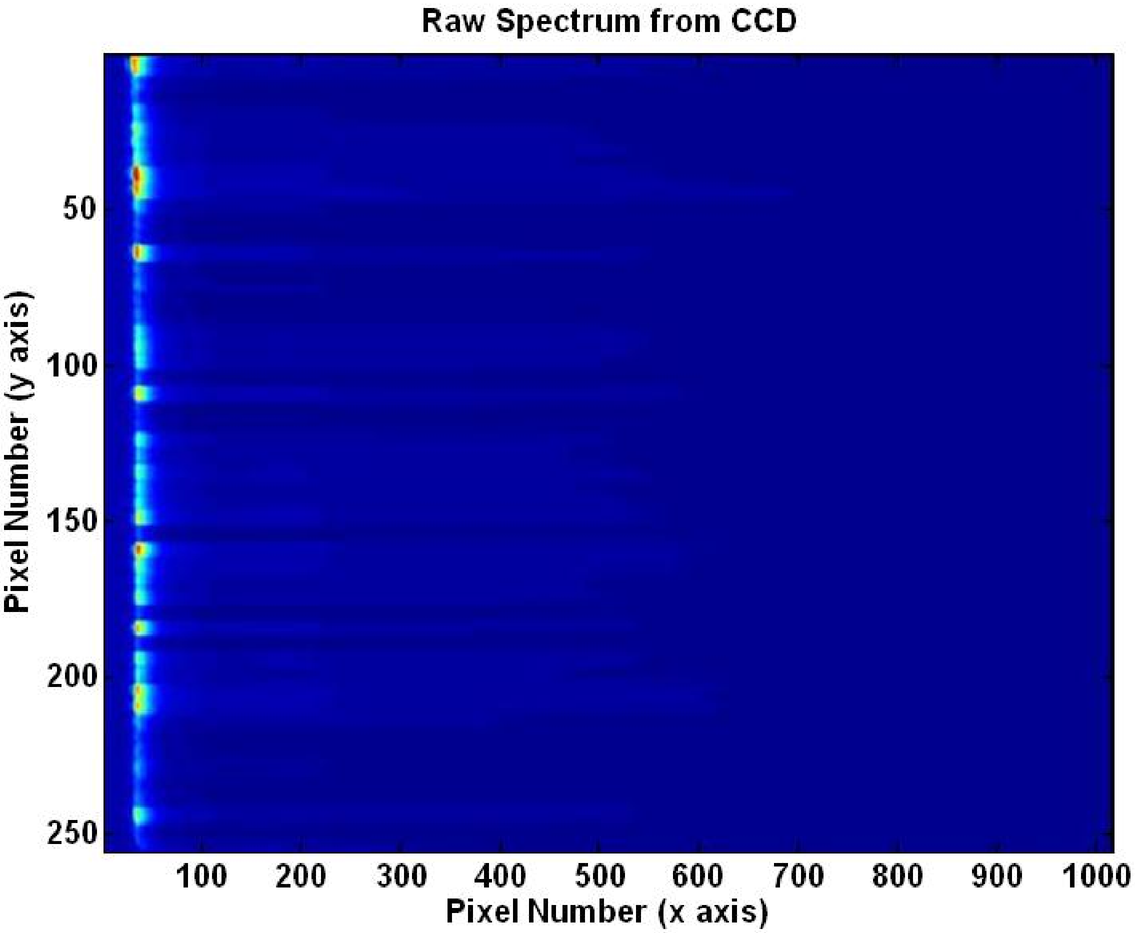

Figure 6. Representative Raman image showing the raw data before processing.

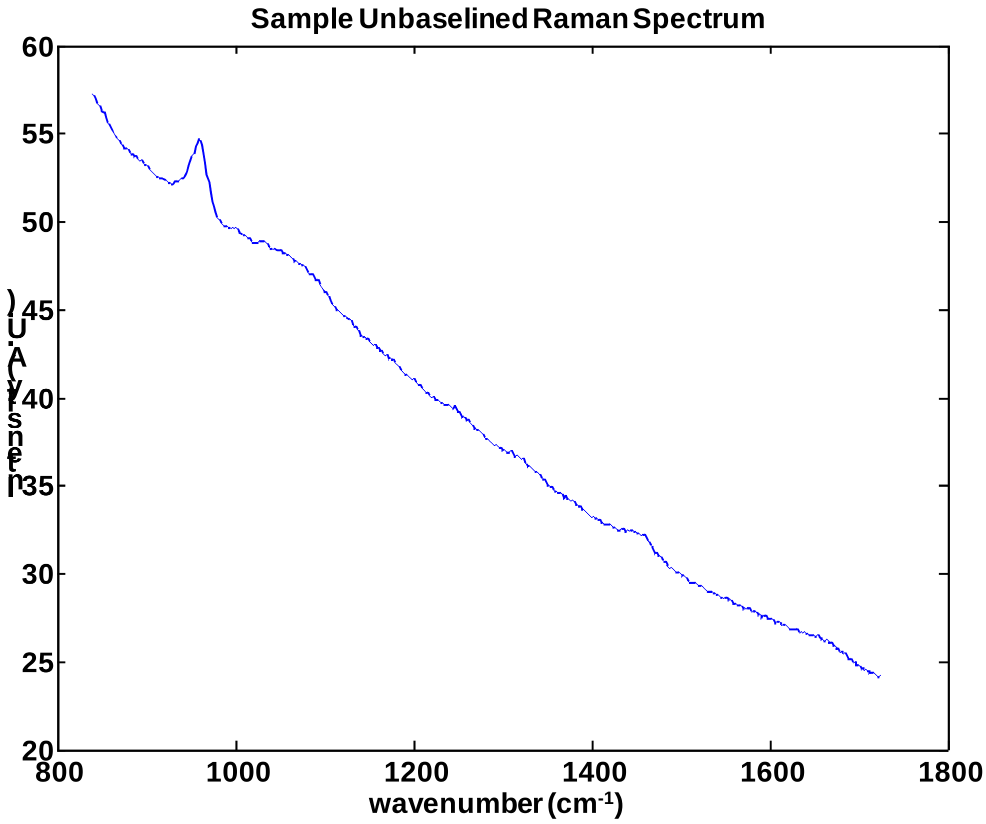

Figure 7. Representative Raman spectrum showing the data truncated to the 838-1723 cm^{-1} spectral region prior to background subtraction.

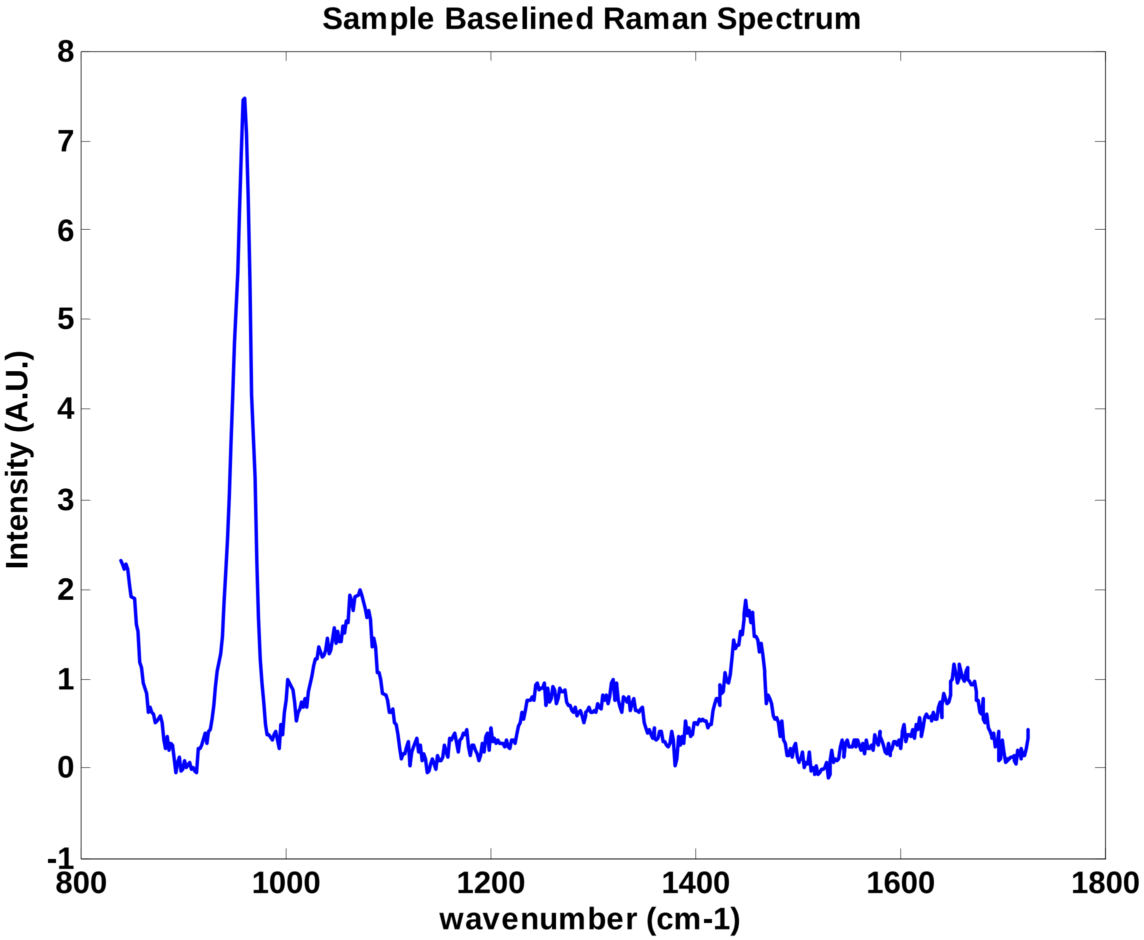

Figure 8. Representative Raman spectrum showing the completely processed data with the fluorescence background removed.

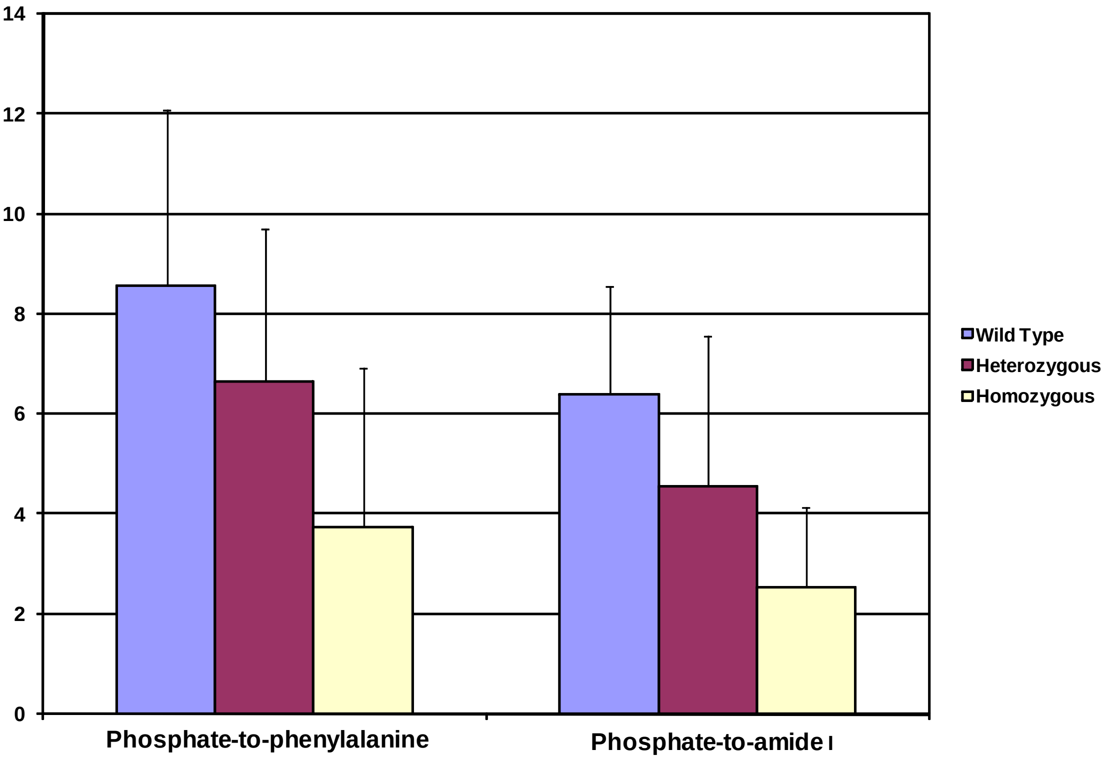

Figure 9. Phosphate-to-phenylalanine and phosphate-to-amide I ratios, with standard deviations, across all three phenotypes.

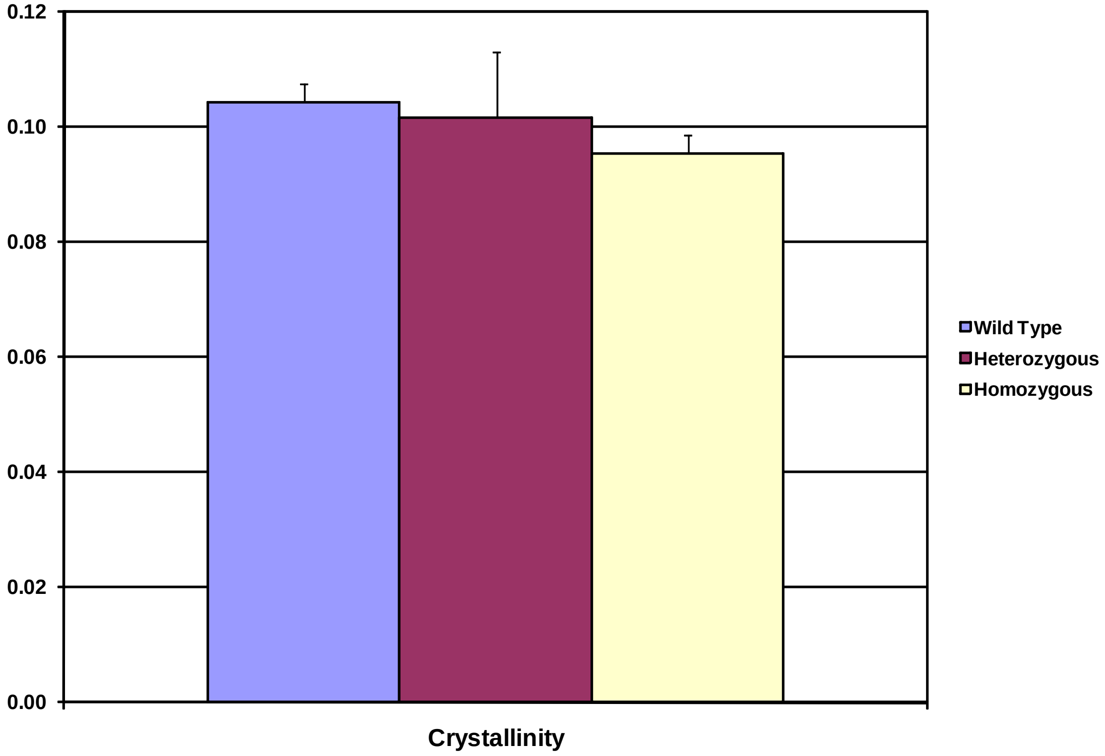

Figure 10. Crystallinity, with standard deviations, across all three phenotypes.

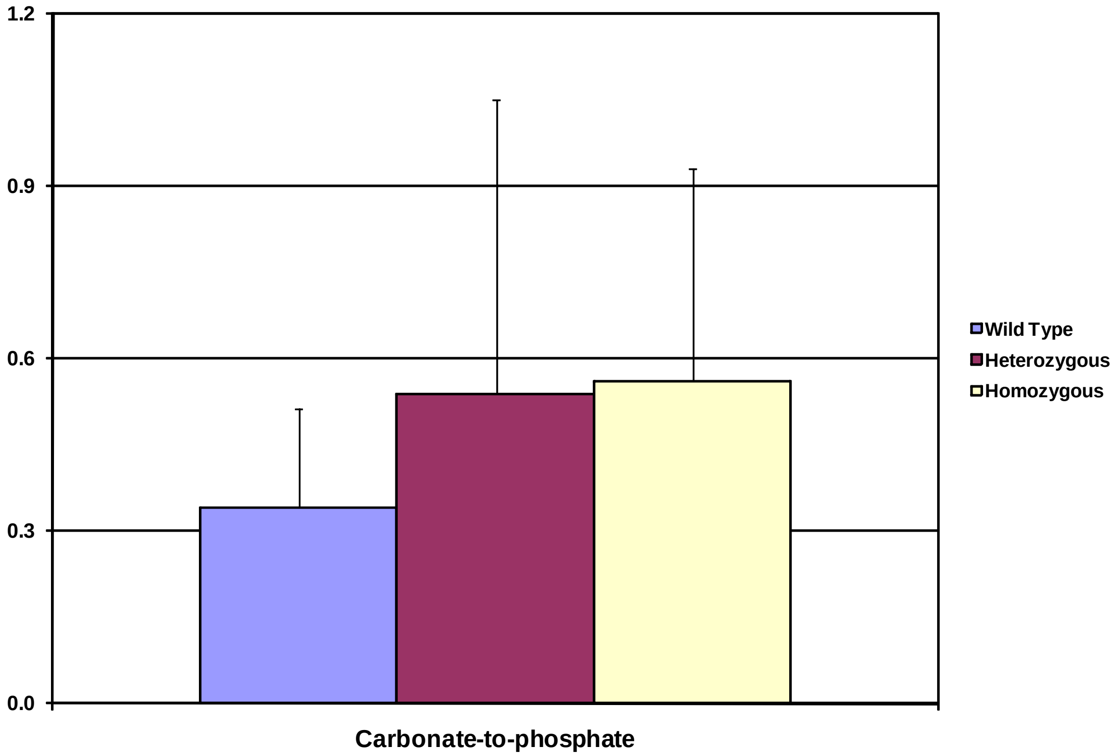

Figure 11. Carbonate-to-phosphate ratio, with standard deviations, across all three phenotypes.

REFERENCES

1. Martin RB, Burr DB, and Sharkey NA. Skeletal Tissue Mechanics. New York: Springer, 1998.
2. Carden A and Morris MD (2000) Application of vibrational spectroscopy to the study of mineralized tissues (review). *J Biomed Opt* 5(3):259-268.
3. Carden A, Rajachar RM, Morris MD, and Kohn DH (2003) Ultrastructural changes accompanying the mechanical deformation of bone tissue: A Raman imaging study. *Calcif Tissue Int* 72(2):166-175.
4. de Carmejane O, Morris MD, Davis MK, Stixrude L, Tecklenburg M, Rajachar RM, and Kohan DH (2005) Bone chemical structure response to mechanical stress studied by high pressure Raman spectroscopy. *Calcif Tissue Int* 76(3):207-13.
5. Morris MD, Finney WF, Rajachar RM, and Kohn DH (2004) Bone tissue ultrastructural response to elastic deformation probed by Raman spectroscopy. *Faraday Discuss* 126:159-68; discussion 169-83.
6. McCreadie BR, Morris MD, Chen TC, Sudhaker Rao D, Finney WF, Widjaja E, and Goldstein SA (2006) Bone tissue compositional differences in women with and without osteoporotic fracture. *Bone* 39(6):1190-5.
7. Kozloff KM, Carden A, Bergwitz C, Forlino A, Uveges TE, Morris MD, Marini JC, and Goldstein SA (2004) Brittle IV mouse model for osteogenesis imperfecta IV demonstrates postpubertal adaptations to improve whole bone strength. *J Bone Miner Res* 19(4):614-22.
8. Young MF and Xu T (2001) Creating transgenic mice to study skeletal function. In: Cowin SC, Ed. Bone Mechanics Handbook. CRC Press: Boca Raton. pp. 4-1 to 4-19.
9. Novince CM, Koh AJ, Brown HA, Hu JC, Rosol TJ, McCauley LK, and Toribio RE (2008) Parathyroid hormone related protein (PTHrP) nuclear localization sequence and C-terminus regulate craniofacial development. *J Bone Miner Res* 23:S74.
10. Toribio RE, Brown HA, Novince CM, Gooding LM, Shu ST, Werbeck JL, McCauley LK, Foley J, and Rosol TJ (2008) Skeletal dysmorphology of mice lacking the mid-region, nuclear localization sequence and C-terminus of parathyroid hormone-related protein. *J Bone Miner Res* 23:S45.
11. Alexander RM. Human Bones: A scientific and pictorial investigation. New York: Pi Press, 2005.

Acknowledgments

I would like to thank Jacqueline Cole for her constant support and mentorship through the project, Dr. Michael Morris for giving me the opportunity, and Chad Novince, Laurie McCauley, and Ramiro Toribio for the specimens. I'd also like to thank Dr. Francis Esmonde-White and Dr. Matthew Schulmerich for help with data analysis. This study was funded through NIH R01 AR047969 and F32 AR056186 (JHC).

APPENDIX A. Specimen list using neutral density filter during Raman measurements

The following specimen were examined using a neutral density filter for measurements:

M9 +/- #2
J9 +/- #2
C10 +/+ #6
M10 -/- #1
C10 +/+ #5
E10 +/-
C8 +/+ #2
B9 -/-
M9 +/- #1

APPENDIX B. MATLAB SCRIPTS

B.1 Index of MATLAB scripts and their data processing functions

preprocessing.m	correct image curvature remove spikes subtract dark current
baselining_and_collating.m	background subtraction (baselining)
mod_GIFTSv2.m	sub-function

Disused scripts

data_process.m	background subtraction (baselining)
solvepeakfit.m	peak fitting
errorfit.m	sub-function
nmsimplex.m	sub-function

B.2 Library of MATLAB scripts

B.2.1 Preprocessing.m

This program prepares the data for baselining and fitting by subtracting dark spectra, white correcting, and establishes the axis calibration using a neon spectrum. For use in MATLAB.

```
% Modified to remove verbose output and eliminate matlab warnings.
%   Francis Esmonde-White and Michael Roberto, June 16 2008
%
% version 0.1 FEW 16/06/2008

% % % % % %
% % % % % % % Preprocess all the data in the subfolders
% % % % % % angleindegrees=-0.68812;
% % % % % %
% % % % % % if all(size(dark)==[1024,128])
% % % % % %     dark=dark(210:1024,2:127);
% % % % % % end
% % % % % % if all(size(white)==[1024,128])
% % % % % %     white=white(210:1024,2:127);
% % % % % % end
% % % % % % if all(size(teflon)==[1024,128])
% % % % % %     teflon=teflon(210:1024,2:127);
% % % % % % end

% load the unspiked hsf file of interest.

% correct the neon
% neon = (neon(1:1024,1:255)-dark)./(white-dark); % now the neon is
      chopped
% to the same range as the data.
neon = (neon-dark)./(white-dark); % now the neon is chopped to the same
      range as the data.
% neon = imrotate(neon', angleindegrees, 'bicubic');
% neon = neon(12:126,3:815);
% francis_uncurve(neon', 'neon');  % needs to be transposed so that it
      runs properly

francis_uncurve(neon, 'neon');
neon=francis_decurve(neon,'neon')';

% francis_uncurve(neon', 'neon', 0.5);
%
% neon = francis_decurve(neon', 'neon')';
% ne = sum(neon(1:255,:));
ne = sum(neon);

% find the neon peaks
[maxy,maxi] = findmaxima(ne);

% load the known wavelength values
cal_vector = xlsread('red3 Calibration.xls');
```

```
% split the loaded values into wavelengths and pixels
wavelen = cal_vector(1,:);
est_pix = cal_vector(2,:);

wavelen(est_pix<5)=[];
est_pix(est_pix<5)=[];

% find the closest pixels
for i=1:numel(est_pix);
    [y,j] = min(abs(est_pix(i)-maxi));
%     disp([i, y]);
    known_pix(i) = maxi(j);
end

% calculate the rshift coefficients
coef =
      wavelen/[known_pix.^3;known_pix.^2;known_pix;ones(size(known_pix)
      )];

% deal with teflon
teflon = (teflon-dark)./(white-dark); % now the neon is chopped to the
      same range as the data.
% teflon = imrotate(teflon', angleindegrees, 'bicubic');
% % % % % teflon = teflon(12:126,3:815);

teflon = francis_decurve(teflon, 'neon')';
tef = sum(teflon);
% tef = sum(teflon(1:255,410:1024));

% initial laser wavelength estimate
laser_wl=829.5;

% iteratively find a better laser wavelength
cm=rshift(1:1024,[coef],laser_wl);
[interp_data,interp_axis]=FEW_interpolate(tef(250:end),cm(250:end),50);
% plot(interp_axis,interp_data); zoom on

[y,i]=max(interp_data);
pos=interp_axis(i);

oldl=nan;

while abs(pos-732)>0.02

    disp(['teflon peak: ', num2str(pos)])
    grandl=oldl;
    oldl=laser_wl;
    if (pos<732)
        % make laser wl bigger
        laser_wl = laser_wl - 0.005;
    else
        % make laser wl smaller
        laser_wl = laser_wl + 0.005;
    end

    if (grandl==laser_wl) % it is jittering around the same point.
        break;
```

```
    end

    % iteratively find a better laser wavelength
    cm=rshift(1:1024,[coef],laser_wl);

      [interp_data,interp_axis]=FEW_interpolate(tef(250:end),cm(250:end
      ),50);
    % plot(interp_axis,interp_data); zoom on

    [y,i]=max(interp_data);
    pos=interp_axis(i);
end

wavenumber_axis = cm;

% preprocess silicon for white correction and dark correction
% si_tmp = (si-dark)'./(white-dark)';

dat=nan(size(data,1),255,1024);

% for each frame in the data images, do the following:
for i=1:size(data,1);

    % subtract the dark and white correct
    dat_tmp = (squeeze(data(i,:,:))-dark60)./(white-dark);

%     tmp=1;
    % rotate the image
%     dat_rot = imrotate(dat_tmp, angleindegrees, 'bicubic');

%     % rotate the image and subtract the silicon background
%     dat_rot = imrotate(dat_tmp-si_tmp, angleindegrees, 'bicubic');

%     dat_rot = dat_rot;
%         dat_rot = dat_rot(1:255,410:1024);

    % uncurve the image
    dat_tmp=francis_decurve(dat_tmp, 'neon')';

%     imagesc(dat_rot(20:100,:))
%     plot(sum(dat_rot(20:100,:)))

    % chop out the portion of interest
    dat(i,:,:) = dat_tmp;

end
```

B.2.2 baselining_and_collating.m

This program truncates and baselines the data using GIFTSv2opt, then collates the data.

```
data_files = dir('mod*spk.mat');

p=0;
for i=1:numel(data_files);
    disp(['file: ',num2str(i)]);


      load(data_files(i).name,'dat','wavenumber_axis','samples','proper
      ties');

    tmp = zeros([size(dat,1),255,541]);

    for j=1:size(dat,1);
        disp(['image: ',num2str(j)]);
        for k=1:255;

      [tmp(j,k,:),baseline]=giftsv2opt(squeeze(dat(j,k,395:935)),4);
        end;
    end

    for j=1:size(dat,1)
        p=p+1;
        [output(p,:),baseline]=giftsv2opt(sum(squeeze(tmp(j,:,:))),1);
        wn_axis(p,:) = wavenumber_axis(395:935);
        samplename(p)=samples(j);
        sampleprop(p,:)=properties(:,j).';
    end
end
```

B.2.3 GIFTS v2_opt.m

This program is a baseline removal script, removing noise of the order specified.

```
function [baselined_spectrum,baseline]=GIFTSv2_opt(raw_spectrum,order)
%LIEBERFIT Baseline removal script based on Applied Spectroscopy, 57, 11, 2003, 1363.
%USAGE: [baselined_spectrum,baseline]=lieberfit(raw_spectrum,order);
%This program applies a multiple least squares baseline curve fitting with
%adjusted parameters to separate Raman and fluorescence features.
%This should reduce strong negative lobes on the sides of peaks.

if size(raw_spectrum,1)>size(raw_spectrum,2)
    raw_spectrum = raw_spectrum';
end

N = numel(raw_spectrum);

% These spectra are "shot noise" limited, so the square root of
% the sum of the counts is the noise, that I am using for an
% error estimate (mvs-this is defined by the noise in the spectra...
% so we need to define a portion in the spectra that has no signal so we can calculate the RMS noise

% We initialize our last spectrum variable, this simplifies our polynomial
% fitting loop
last_spectrum=raw_spectrum;

% to use polyfit we need an x-axis
% this loop generates an x-axis
dummy_x=1:N;

% Fit the spectrum with a polynomial of order N
% This is the first fitting pass
%this polyfit function is self scaleing and self centering
[P,S,MU]=polyfit(dummy_x,last_spectrum,order);

% Generate the values for the curve that was generated by the
% polynomial fit
dummy_based=polyval(P,dummy_x,[],MU);

% initialize some variables
j=1;
convergence=0;
%%%%%%%%%%%%%%%%%%%%%%%%%%%%%%%%%%%%%%%%%%%%%%%%%%%%%%%%%%%%%%%%%%%%%%%%%%%%%%%%%%%%%%%%%%%
%%%mvs so her I will start a counter to determine how many points are reassigned

zero_spectrum = zeros(size(last_spectrum));

% This is the loop where we compare our curve to the spectrum
```

```
while(convergence==0);%, %while we haven't converged
    tmp=find(dummy_based>0);
   KEPT = sum(dummy_based(tmp) <= last_spectrum(tmp));
   DUMP = sum(dummy_based(tmp) > last_spectrum(tmp));

   last_spectrum = min([dummy_based; last_spectrum]);
   last_spectrum = max([last_spectrum; zero_spectrum]);

   % Re-fit and re-generate the values for the fit curve
   [P,S,MU]=polyfit(dummy_x,last_spectrum,order);

    dummy_based=polyval(P,dummy_x,[],MU);

   % here is where we decide if we are done fitting, as an estimate of
      when we
   % should stop when the relative standard deviation of the polynomial
      is less than
   % or equal to the Relative RMSnoise in the measurement

   if  KEPT>=25*DUMP || j>=100; %converges when the difference between
      the fit and the previous fit is less than .0004%
       convergence=1;
%        disp(j);
   end;
   j=j+1; %increment the number of iterations
   %disp(j); %some output to let us know we are running ok

end;

% we calculate the baselined spectrum and return the baseline
baselined_spectrum=raw_spectrum-dummy_based;
baseline=dummy_based;

% let us know we have finished normally
% disp 'finished';

% plot(baselined_spectrum)
% hold on;
% plot(baseline,'r')
% plot(raw_spectrum,'g')

% plot the baselined spectrum
%plot(baselined_spectrum);
```

B.2.4 data_process.m

This was a failed baselining program, which had problems with offset because of low scaled values in the data. This was replaced by baselining_and_collating.

```
files = dir('mod_*_spk.mat');

for i=1:numel(files)
    disp (['file ',files(i).name]);
    save temp.mat files i;
    load(files(i).name);

    for j=1:size(dat,1)
        disp(['spectrum number ',num2str(j)]);
        tmp=squeeze(dat(j,:,395:935));
        for k=1:255;
            if (mod(k,50)==0)
                disp(['row number ',num2str(k)]);
            end
            [baselined,base]=GIFTSv2_opt(tmp(k,:)',4);
            final_data(j,k,:) = (tmp(k,:)-base);
        end
    end

    load temp.mat;
    save(['proc_',files(i).name]);
    clear;
    load temp.mat;
end
```

B.2.5 solvepeakfit.m

This was a fitting program used early in the experiment, replaced by GRAMS. This program uses a Nelder-Meade simplex fitting program, based off their famous paper. Called functions are listed below.

```
% solve for peak fit

% generic

initialoptim.peakcount=;

initialoptim.background.enable=false;

i=

initialoptim.peak(i).enable=true;
initialoptim.peak(i).params= % [ Centre Amplitude Gauss_width
      Lorz_width ]
initialoptim.peak(i).llim=
initialoptim.peak(i).ulim=




% %
number_samples= size(normalized,1);
newheights=zeros(3,number_samples);
fits = zeros(number_samples,i*4);
error = zeros(number_samples,2);

for j=1:number_samples

    region =
    axis = wn_axis(j,region);
    data = normalized(j,region);

    clear p llim ulim

    for i=1:initialoptim.peakcount
        p(i,:)=initialoptim.peak(i).params;
        llim(i,:)=initialoptim.peak(i).llim;
        ulim(i,:)=initialoptim.peak(i).ulim;
    end
    %         err=errorfit(p, axis, data, llim, ulim)

    input=p.';
    input=input(:);

    llim=llim.';
    llim=llim(:);

    ulim=ulim.';
    ulim=ulim(:);
```

```
% set initial parameters
i=1;    input((i-1)*4+2)=data(11)*2;
i=2;    input((i-1)*4+2)=data(20)*2;
i=3;    input((i-1)*4+2)=data(32)*2;

input=(input-llim)./(ulim-llim);
input=-log((1-input)./input);

[p,err]=nmsimplex(input.', @errorfit, axis, data, llim.', ulim.');
p=mean(p);
% pnew = (1./(1+exp(-p(1,:).'))).*(ulim-llim)+llim;
pnew=(1./(1+exp(-p.'))).*(ulim-llim)+llim;

fits(j,:)=pnew;

peaks = reshape(pnew,[4,3])'

% plot out fit versus the raw data
y=zeros(size(axis));
numpeaks=numel(p)/4;
% pnew = (1./(1+exp(-p))).*(ulim-llim)+llim;

for i=1:numpeaks
    %     if optim.peak(i).enable
    % %         p=optim.peak(i).params;
    % %
    % %         llim=optim.peak(i).llim;
    % %         ulim=optim.peak(i).ulim;

    %         p(i,:)

    y=y+voigtprofile(axis,pnew((i-1)*4+(1:4)));


    %     end
end

hold off;
plot(axis,data,'b')
hold on;
plot(axis,y,'r')
disp(['sample is ',num2str(j)])
pause(0.5);


for i=1:numpeaks
    %     if optim.peak(i).enable
    % %         p=optim.peak(i).params;
    % %
    % %         llim=optim.peak(i).llim;
    % %         ulim=optim.peak(i).ulim;

    %         p(i,:)
```

```
        newheights(i,j)=voigtprofile(pnew((i-1)*4+1),pnew((i-
      1)*4+(1:4)));

        %     end
    end
    error(j,:)=[mean(err),sqrt(sum((err-mean(err)).^2)/(numel(err)-
      1))];

    % err=errorfit(optim,axis,data)

end

% FWHM for the phosphate 959 peak
% fits(:,12) is the Lorentzian width
% fits(:,11) is the Gaussian width
fwhm = 0.5346*fits(:,12)+sqrt(0.2166*fits(:,12).^2 + fits(:,11).^2);
```

B.2.6 errorfit.m

```
function err=errorfit(p, axis, data, llim, ulim)

% if optim.background.enable
%     y = polyval(optim.background.coeffs,axis);
% else
%     y=zeros(size(axis));
% end

y=zeros(size(axis));

numpeaks=numel(p)/4;
pnew = (1./(1+exp(-p))).*(ulim-llim)+llim;

for i=1:numpeaks
%     if optim.peak(i).enable
% %         p=optim.peak(i).params;
% %
% %         llim=optim.peak(i).llim;
% %         ulim=optim.peak(i).ulim;

%         p(i,:)
         y=y+voigtprofile(axis,pnew((i-1)*4+(1:4)));

%     end
end
% hold off;
% plot(axis,data,'b')
% hold on;
% plot(axis,y,'r')
% pause(0.001);
err = sqrt(sum((data-y).^2));



function [y]=voigtprofile(x,p)
% Based on the function voigt.m from the mfit toolbox by:
%
% Author:  MZ <mzinkin@sghms.ac.uk> adapted from DFM
% Description:  Voigt
%
%
% Francis Esmonde-White, April 2009



% voigt     : Voigt
% function [y, {name, pnames, pin}]=voigt(x,p, {flag})
%
% MFIT Voigt fitting function
% p = [ Amplitude Centre Gauss_width Lorz_width Background ]

% Author:  MZ <mzinkin@sghms.ac.uk> adapted from DFM
% Description:  Voigt
```

```
% p = [ Centre Amplitude Gauss_width Lorz_width ]
% % p = [ Amplitude Centre Gauss_width Lorz_width Background ]
%
% 1->2
% 2->1
%
% 5 is removed

% if nargin==2;
    N = 16;
    b = -sqrt(log(2))/p(3);
    a = b*p(4);
    b = b*2*i;
    z = a + b*(x-p(1));

    M=2*N; M2=2*M; k=[-M+1:1:M-1]';
    L=sqrt(N/sqrt(2));
    tt=(L*tan(k*pi/M2)).^2;
    f=[0; exp(-tt).*(L^2+tt)];
    a=real(fft(fftshift(f)))/M2;
    a=flipud(a(2:N+1));
    l=L-z;
    Z=(L+z)./l;
    pp=polyval(a,Z);
    y=p(2)*real(2*pp ./l.^2+(1/sqrt(pi))*ones(size(z)) ./l);
```

B.2.7 nmsimplex.m

```
function [P,Y]=nmsimplex(Pinit,solver,varargin)

% NMSimplex
%
%
% Nelder-Meade Simplex
%  J. A. Nelder, R. Mead, The Computer Journal 1965, 7, 308.
%
% Francis Esmonde-White, Sepember 4 2008, version 0.1

% n variables
% P points defining the current simplex [n+1]

% Estimated number of iterations (i) to convergence based on the number
      of
% variables (k)
% i = 3*16*(k+1)^(2*11);

% Constants:
randomization_constant = 1000; % the inverse of this value determines
      the distance to look around the current values.
alpha = 1.01; % alpha is a positive constant, reflection coefficient
gamma = 1.95; % gamma is a positive constant greater than unity
beta = 0.49; % beta is the contraction constant between 0 and 1
termination_error = 1e-7; % take this as the standard deviation of the
      spectrum multiplied by the number of points.

maxiters = 20000; % give up and run away if we hit this point.

% ENTRY: Calculate initial Pi and Yi

% input Pinit
n = numel(Pinit);
P = repmat(Pinit,[(n+1),1]);
tmp = randn(size(P));
tmp(1,:)=0;
P = (P+0.01).*(1+tmp/randomization_constant);

for i=1:(n+1);
    Y(i) = solver(P(i,:),varargin{:});
end

iters = 0;
minimum_found = false;
while ~minimum_found
    iters=iters+1;
    if iters>maxiters
        break;
    end

    % Determine h, l
    [garbage,h] = max(Y);
```

```
[garbage,l] = min(Y);

% Calculate Pcentroid
Ptemp = P;
Ptemp(h,:)=[];
Pcentroid = mean(Ptemp);

% replace P(h,:) by a new point.

% reflection (of the worst point through the centroid)
% alpha is a positive constant, reflection coefficient
Pnew = (1+alpha)*Pcentroid - alpha*P(h,:);
Ynew = solver(Pnew,varargin{:});

if (Ynew < Y(l))
    % expansion (of Pnew through the centroid)
    % gamma is a positive constant greater than unity
    Pnew2 = gamma*Pnew + (1-gamma)*Pcentroid;
    Ynew2 = solver(Pnew2,varargin{:});

    if (Ynew2 < Y(l))
        P(h,:)=Pnew2;
        Y(h)=Ynew2;
    else
        P(h,:)=Pnew;
        Y(h)=Ynew;
    end
else
    Ytmp = Y;
    Ytmp(h)=[];
    if ~all(Ynew>Ytmp)
        P(h,:)=Pnew;
        Y(h)=Ynew;
    else
        if (Ynew<=Y(h))
            P(h,:)=Pnew;
            Y(h)=Ynew;
        end
        % contraction (of P(h,:) towards the centroid)
        % beta is the contraction constant between 0 and 1
        Pnew2 = beta*P(h,:) + (1-beta)*Pcentroid;
        Ynew2 = solver(Pnew2,varargin{:});
        if (Ynew2 > Y(h))
            for i=1:(n+1);
                P(i,:)=(P(i,:)+P(l,:))/2;
                y(i) = solver(P(i,:),varargin{:});
            end
        else
            P(h,:)=Pnew2;
            Y(h)=Ynew2;
        end

    end
end
```

```
    stderr = sqrt(sum((Y-mean(Y)).^2)/n);

    if (stderr < termination_error)
        % this relies on the difference between the solution values of
      the different vertices
        minimum_found = true;
    end
end

disp(iters)
```